

Influence of coronary plaque morphology on local mechanical states and associated in-stent restenosis

Janina C. Datz^{a,b,*}, Ivo Steinbrecher^c, Johannes Krefting^b, Leif-Christopher Engel^b, Alexander Popp^c, Martin R. Pfaller^d, Heribert Schunkert^b, Wolfgang A. Wall^{a,e}

^a*Institute for Computational Mechanics, Technical University of Munich, Germany*

^b*Department of Cardiology, TUM University Hospital German Heart Center, Technical University of Munich, Germany*

^c*Institute for Mathematics and Computer-Based Simulation, University of the Bundeswehr Munich, Germany*

^d*Biomedical Engineering, Yale University, USA*

^e*Munich Institute of Biomedical Engineering, Technical University of Munich, Germany*

Abstract

In-stent restenosis after percutaneous coronary intervention is a multifactorial process. Specific morphological lesion characteristics were observed to contribute to the occurrence of in-stent restenosis. Local mechanical factors, such as stresses and strains, are known to influence tissue adaptation after stent implantation. However, the influence of morphological features on those local mechanical states and, hence, on the occurrence of in-stent restenosis remains understudied. This work investigates the correlation between local mechanical quantities and in-stent restenosis by evaluating the stress distributions in the artery wall during and after stent implantation for informative lesion morphologies. We perform computational simulations of the stenting procedure with physics-based patient-specific coronary artery models. Different morphologies are assessed using the spatial plaque composition information from high-resolution coronary computed tomography angiography data. We quantify the correlation between in-stent restenosis and local tensional stresses. We found that specific morphological characteristics like circumferential or asymmetric block calcifications result in higher stresses in the surrounding tissue. This study concludes that local stresses are critical for assessing the individual in-stent restenosis risk.

Keywords: Coronary artery disease, in-stent restenosis, patient-specific modeling, computational simulation, coronary angioplasty

*Corresponding author

Email address: janina.datz@tum.de (Janina C. Datz)

1. Introduction

Percutaneous coronary intervention (PCI) with stent implantation is the most frequently used treatment for flow-limiting plaques in coronary arteries. However, in up to 10% of treated lesions, in-stent restenosis (ISR), i.e., a re-occlusion of the vessel by more than 50% of the initial lumen, is diagnosed at follow-up after 6-12 months [1]. The occurrence of ISR depends on a complex interplay between patient-, lesion-, and procedural-specific factors [2]. A thorough assessment of a lesion’s risk for stenting complications is crucial for choosing an appropriate lesion preparation technique, determining the optimal treatment strategy, and planning follow-up examinations. However, the known risk factors are insufficient to predict ISR reliably. Importantly, individual physical properties of the lesion are currently not considered. Coronary imaging, such as optical coherence tomography (OCT) or intravascular ultrasound, has become increasingly important in PCI in assessing complex lesions and gathering more information about individual lesion characteristics. Observational clinical studies suggest that specific lesion morphologies influence the ISR risk [3–8]. Utilizing lesion morphology information could add a key element to the traditional risk assessment factors.

The currently known risk factors for ISR in clinical guidelines were determined in large-scale clinical studies. For instance, a small target vessel size or increased stented length were found to be independent predictors for ISR [2, 9]. While these studies found strong correlations between lesion-specific characteristics and the occurrence of ISR, local mechanical factors, i.e., continuum metrics such as stress, strain, stiffness, or internal elastic energy, were not considered.

During PCI, the artery tissue undergoes large stretches beyond its normal physiological domain, which can promote inflammatory pathways that serve as a stimulus for the formation of neointimal tissue and restenosis [10–12]. Additionally, it has been shown that changes in the mechanical state strongly affect vascular growth mechanisms, as cell and matrix turnover and growth mechanisms work towards restoring the tissue’s natural mechanical homeostasis, i.e., the set point of the tissue’s preferred mechanical state [13, 14]. The mechanical state is sensed by cells, and deviations from the homeostatic targets stimulate modifications in their phenotype and extracellular matrix [15, 16]. Hence, significant elevations of the stress values above a critical threshold outside the normal physiological range influence growth and remodeling processes.

Local material properties in diseased coronary arteries differ depending on the individual plaque composition. Lipid-rich tissue is a soft, fatty material; fibrous plaque tissue is generally stiffer, and calcified tissue behaves rigidly. It has been shown that the plaque composition and morphology influence the mechanical state during PCI [17, 18]. Furthermore, several studies suggest a connection between the clinical outcome and the plaque morphology. Morphological characteristics of the plaque include specific structural features, such as the location, shape, and size of different plaque components. For instance, circumferential or convex calcifications, eccentric plaque, and the “headlight sign”, i.e., blocks of calcium on opposing sides of the vessel cross-section, have been observed to pose

a high risk for stent underexpansion and ISR [3–5]. Clinical studies on the role of advanced plaque features, including the coronary calcium extent, position, morphology, and density, were reviewed regarding the risk of acute coronary events [6], ischaemia [7], and PCI complications [8]. The latter concluded that detailed plaque characterization is crucial for tailored and optimized PCI interventions. However, the correlation between plaque morphological features, their influence on the tissue’s mechanical state, and the associated clinical outcome remain underexplored.

Computational modeling is well established for studying structural mechanics in PCI. Different approaches for finite element simulations of the stenting procedure in patient-specific coronary artery models have been proposed by [19–27]. However, information about the plaque morphology, which is critical for predicting stress distributions, was not included.

The impact of the overall plaque type, i.e., cellular, hypocellular, or (partially) calcified, on the lumen gain and resulting wall stresses during PCI was shown in generic artery models [28–32]. Generic artery models with spatially distinguished plaque materials were used in [33–36], demonstrating the effect of different plaque morphologies. However, the characteristics of realistic arteries differ significantly from generic plaque models. Recent studies used 2D and 3D patient-specific models to study the influence of the plaque composition or morphology on the stenting outcome [37–41]. However, since the plaque compositions were not spatially resolved, they only assessed the influence of the individual plaque composition but not the pathoanatomical context.

In normal loading conditions, the spatially resolved plaque composition was included in the models to assess the plaque vulnerability [42–46]. In [47], the influence of the specific plaque morphology on the mechanical response was studied. However, these studies did not assess the mechanics during or after stenting. For the simulation of PCI, the spatially resolved plaque morphology was considered in [48–51], focusing on the realistic stent implantation through pre- and post-stenting imaging validation. In [52], the impact of heavy calcifications on the stenting outcome was studied. The effects of separate plaque components in carotid arteries were analyzed in [53]. However, the influence of specific morphological plaque features on the stress state during and after PCI and the clinical outcome regarding ISR has not been assessed yet and is studied in this paper.

In previous computational modeling studies, the plaque composition and morphology information was often retrieved from histology [39, 54, 55], magnetic resonance imaging (MRI) [38, 53], or OCT [40, 41, 48–52]. However, histology and MRI cannot assess coronary arteries in-vivo. OCT requires mapping to a centerline using angiography data, or it can only be used in artificially straightened artery models. Coronary computed tomography angiography (CCTA) is an emerging non-invasive imaging technology that enables the fast acquisition of a high-resolution, 3D image of the coronary arteries. Most notably, it can quantify of the plaque extension, volume, and composition [56]. The tissue absorbance determines the grey value of the CCTA image, so-called Hounsfield-Unit (HU), which can be used to distinguish the components of coronary atherosclerotic

lesions [57, 58]. The mapping from the HU value to the distinct component can be performed using fixed thresholds or adaptive algorithms, such as Gaussian Mixture Model (GMM) clustering [59]. The latter method accounts for the CCTA limitation of different kilovoltage settings and acquisition parameters, which makes a unique comparison of plaque characteristics with fixed thresholds problematic [57]. Threshold- or GMM-based clustering of CCTA-based plaque information correlates well with established plaque analysis techniques [60–63].

This work analyzes the influence of specific plaque morphological features on the clinical outcome based on the hypothesis that local mechanical states are an important driving factor for ISR. We use computational modeling of the stenting procedure to assess stresses on the vessel wall during and after PCI. The individual plaque morphology is included in the computational models using a GMM-based mapping from CCTA imaging data. We present four relevant example lesions from clinical cases with different morphological features; the respective angiography and catheter laboratory data are used to set up the stenting simulations. We correlate the stresses after PCI with the clinical outcome of the follow-up examination, assessing stress thresholds critical for ISR initiation. We compare the stress distributions at specific plaque morphological features and identify features and locations leading to higher local stresses.

2. Methods for patient-specific coronary artery modeling

The computational models and methods to simulate PCI in patient-specific coronary arteries were proposed in the authors’ previous publication [20]. In the following section, we introduce the inclusion of plaque composition information from CCTA imaging into the patient-specific models and summarize the simulation setup.

2.1. Plaque composition mapping from CCTA

The artery comprises three layers, i.e., the intima, tunica media, and adventitia, which are modeled as separate continua. Details on the model generation and materials are given in Appendix A. The intima is further heterogeneously classified into the plaque components: lipid-rich tissue, fibrotic tissue, normal (healthy) intimal tissue, and calcifications. Figure 1 shows the components of the patient-specific artery model for an exemplary section.

We assume that the HU value of a plaque component is not necessarily within one fixed range but can instead be represented by a Gaussian distribution. The lesion is composed of a linear combination of these distributions, i.e., the Gaussian distributions of the components can overlap. This overlapping can be attributed to the fact that the plaque components transform continuously on a microstructural level. To cluster the components with adaptive thresholds, we use a Gaussian Mixture Model (GMM) segmentation. A GMM is a probabilistic model that assumes the data is a mixture of Gaussian distributions with unknown parameters [59]. The GMM is constructed from the HU data of the intima and initialized with the typical values for the plaque components

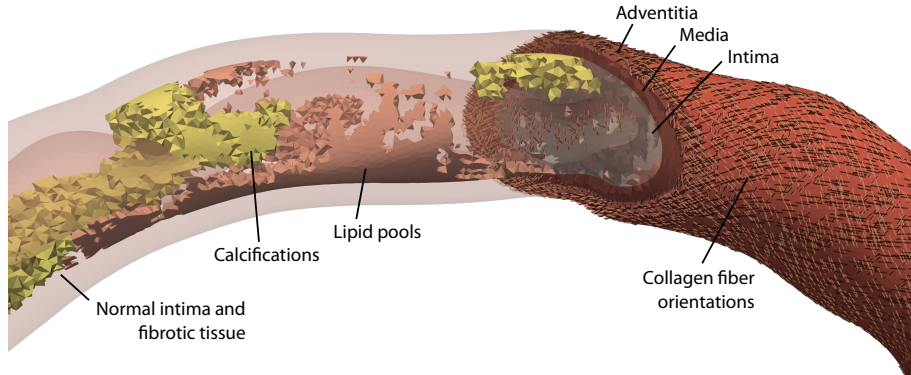


Figure 1: Extract of a patient-specific coronary artery model. The fibrotic tissue and normal intima are not shown for a better overview.

taken from [58]. Each HU value is assigned to a component using the GMM mapping. Figure 2 shows the GMM on the histogram plot of the intimal tissue of an exemplary lesion.

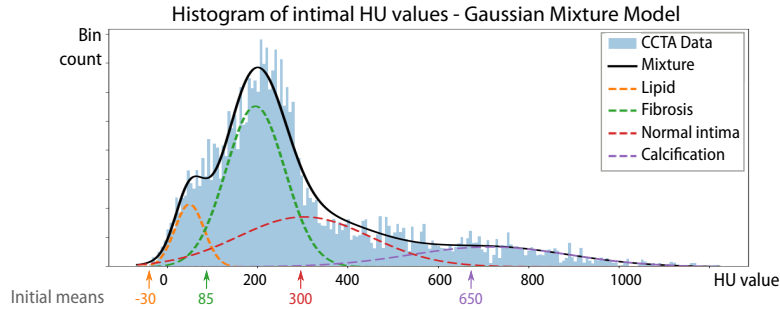


Figure 2: Gaussian Mixture Model (GMM) for the plaque tissue of an exemplary lesion. Light blue: CCTA data; Gaussians of the different components and their initial means, i.e., the pre-defined mean values for each component, are shown in yellow, green, red, or purple for lipid-rich tissue, fibrosis, normal intimal tissue, or calcifications, respectively. Black line: Mixture of all components.

This approach considers the whole 3D geometry for the plaque segmentation. Instead of viewing the cross-section slices individually, the segmentation also contains information about the axial dispersion of the plaque. The 3D modeling of the plaque enables a realistic representation of the plaque morphology, which is crucial for assessing the influence of specific plaque features on local stresses. The segmentation of an exemplary lesion is shown in Fig. 3 on a cross-sectional slice. Details on the tools and specifications of the GMM-based mapping are given in Appendix B.

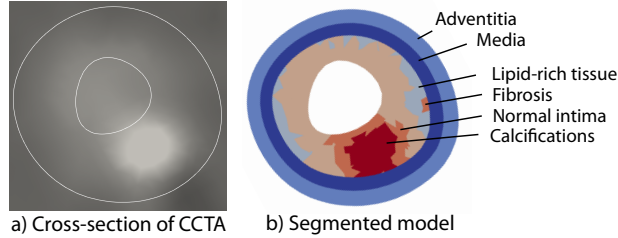


Figure 3: Plaque segmentation of an example lesion. a) Cross-section of the CCTA image orthogonal to the vessel centerline with initially segmented outlines. b) Same slice in the clustered model with assigned plaque components

2.2. Percutaneous coronary intervention simulation

The structure mechanics simulations employ finite element methods based on the underlying physics equations, i.e., balance equations, constitutive relations, and the respective boundary conditions, and are done in our in-house open-source multiphysics high-performance code 4C [64]. For details on the simulation methods and background, the reader is referred to [20]. Here, we only summarize the main points.

We employ a simplified model for the coronary balloon catheter and reduced-dimensional models for the balloon-expandable stents. The stent geometry is based on the “corrugated rings” design (see, e.g., [65]), and modeled with [66]. It is shown in Fig. 4c). The edges are rounded, resulting in a more realistic expansion shape compared to [20]. The material follows an elastoplastic constitutive law. The stenting device is positioned based on the coronary angiography imaging data, shown exemplarily for one lesion in Fig. 4. The initial configuration of the stenting device is assumed to be stress-free.

Furthermore, recently developed methods for the mixed-dimensional contact interaction between the stenting device and the artery are employed [67]. We prescribe a pressure boundary condition to the inner surface of the balloon, leading to its radial expansion. The ends of the balloon and the cut-off surfaces of the artery model are fixed using spring-dashpot boundary conditions. The stent ends are fixed to allow only radial expansion, preventing the stent from moving in the axial direction. The mechanical equilibrium is described without inertial forces; we use a quasi-static pseudo-time discretization and apply the loads in small time steps.

3. Patient-specific simulations

In the following, we present the computational simulation of the stenting procedure on four lesions based on clinical cases from the TUM University Hospital German Heart Center. We use the coronary angiography and catheter laboratory data to assess the patient demographics, lesion specifications, and details about the type of intervention and outcome. The CCTA data is the basis for the model geometry and morphology, as detailed in Section 2. We assess the

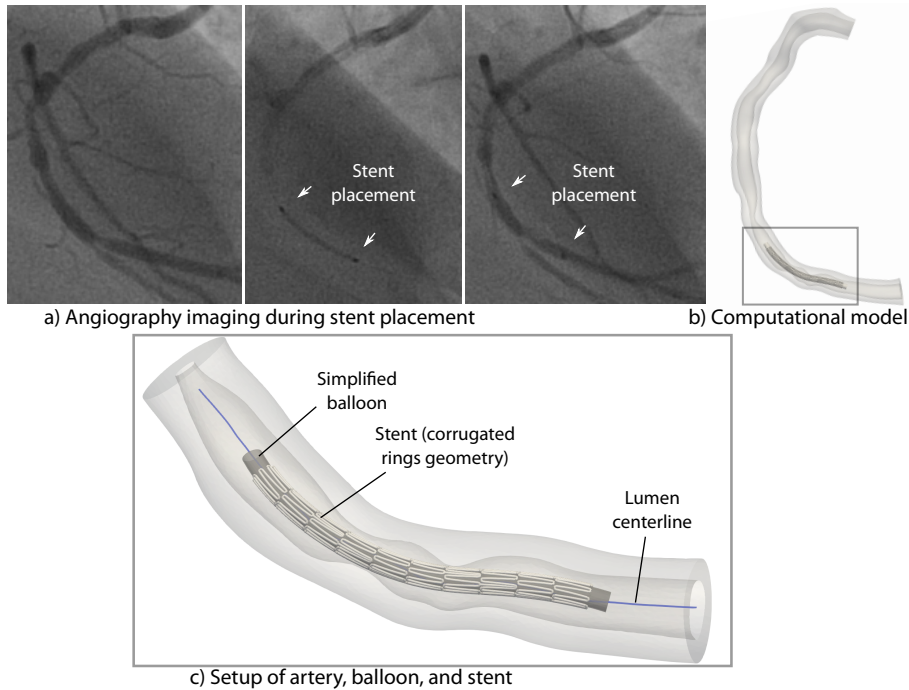


Figure 4: Stent placement in the computational model guided by the angiography imaging during the intervention

stress distributions in the artery wall during the maximum balloon expansion and the remaining stresses after the stenting.

3.1. Patient selection and medical data

We selected the example lesions based on their specific morphological plaque features. For all assessed lesions, coronary artery disease was diagnosed and treated with coronary angioplasty and stent implantation. Follow-up angiographic imaging revealed whether ISR had occurred in the stented region and if it was focal (between stents, at the stent edges, or the stent body), multifocal, or diffuse. Table C.2 in Appendix C summarizes the patient demographics, diagnosis, prior cardiovascular risk factors, treatment in the catheter laboratory, and the outcome at the follow-up after 6-12 months. For this study, we chose lesions that share a diagnosis (CAD in at least one right coronary artery segment) and treatment (angioplasty with stent implantation) for better comparability. Figure 5 shows the four selected lesions, highlighting the specific calcification characteristics and the clinical outcome at follow-up.

3.2. Stress distribution after the intervention

PCI with stent implantation is simulated as described in Section 2. We assess the mechanical state after the PCI, i.e., after the balloon withdrawal. Concisely,

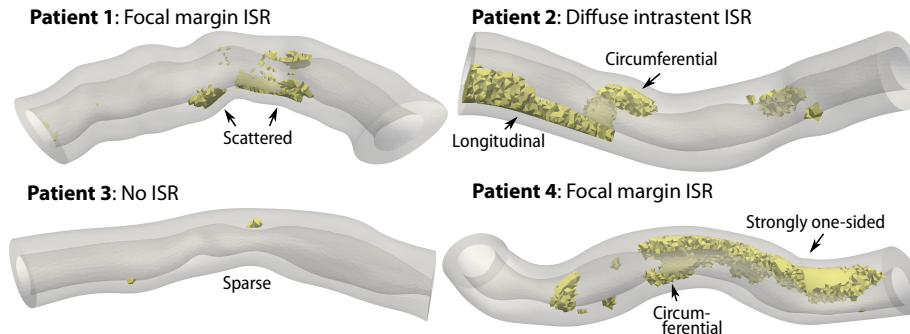


Figure 5: Lesion sections of sample patients with calcification patterns (yellow).

we review the first principal stresses, i.e., the stress values in the direction of the maximum tensional stress, as relevant mechanical value for vascular growth and remodeling [68]. Although tissue strains are also relevant for adaptation, we focus on stresses as they inherently account for both mechanical loading and material properties. Appendix D shows the stent placement, final stented artery, and a comparison of high-stress locations with the clinical follow-up angiography results in detail for each patient.

At the maximum balloon expansion, we observe peak tensional stresses of 120 kPa. After the balloon withdrawal, the tensional stresses peak at around 30-60 kPa. Figure 6 summarizes the high-stress and ISR locations in the angiography for the four example lesions. The threshold values for the simulation results are determined based on the overall stress values: The first threshold (light red) shows the top 20% of the remaining stresses after PCI in the respective numerical example; the second threshold shows the top 5% (dark red). For Patient 1, no follow-up imaging was available, but only the clinical classification as focal margin ISR. From the remaining images, we observe a correlation between the high-stress locations after the stent simulation and the ISR regions seen in the angiography images. The simulation of Patient 3 shows no significant stress elevations in the stented area; the respective follow-up angiography also shows no signs of ISR. The simulated results comply well with the lumen gain, as seen in the angiography.

The areas of peak stress highly depend on the plaque morphology. In Patient 1, the lesion consists of mainly fibrotic and normal intima tissue with a small amount of scattered calcifications. The highest stresses are reached at the stent boundaries and in the most stenotic section. Patient 2 shows exceptionally high stresses in the proximal area, where a specific calcification pattern switches from a longitudinal shape to winding around the lumen. Additionally, elevated stress levels can be observed at the distal stent boundary. In the mainly fibrotic lesion of Patient 3, which did not show signs of ISR in the clinical follow-up, we simultaneously observed only mildly elevated stresses around the narrowest lumen area. Patient 4 shows high stresses at the stent boundaries and in the

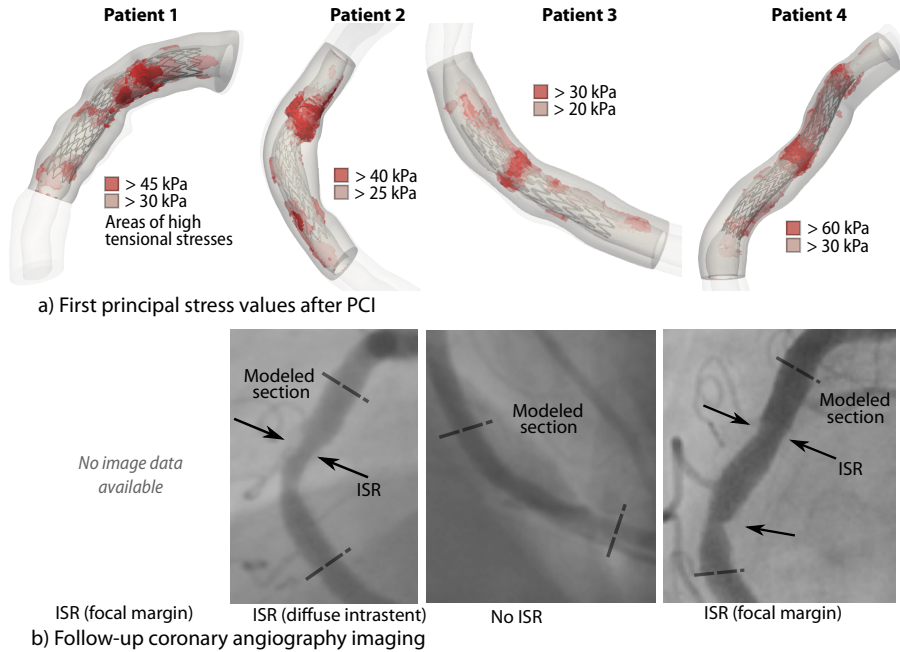
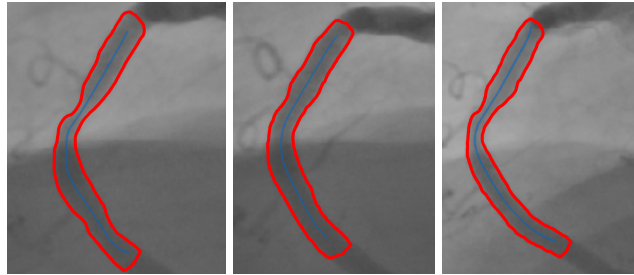


Figure 6: Comparison of a) regions of high tensional stress after PCI simulation and b) angiography images at follow-up

middle section, where the calcification pattern forms a circumferential pattern around the lumen.

3.3. Correlation between restenosis and stresses

We present a regional analysis of the artery diameters before stenting, after stenting, and at the follow-up angiography to quantify the correlation between the tensional stresses along the centerline and the amount of restenosis. For this analysis, we segment the end-diastolic frames of the angiography data using the open-source deep learning tool *AngioPy*, which was trained for coronary segmentation [69], see Fig. 7a). Since no reference scale is available in the angiography images, we scale the segmented diameters to the diameter proximal to the stented region, assuming that the diameter stays approximately unaltered in this area. We approximate the percentage of regional restenosis using the diameter data after the stenting and at the follow-up angiography (dashed lines). To match the datasets to the same section of the centerline, the maximum inscribed sphere diameter of the CCTA-based model and the diameters of the angiography data prior to the intervention are used, see Fig. 7d) (dotted lines). However, a quantitative comparison of CCTA and angiography data is difficult due to the different image acquisition techniques. Using the same scaling, the integrated stresses along the centerline are compared to the ISR percentage.

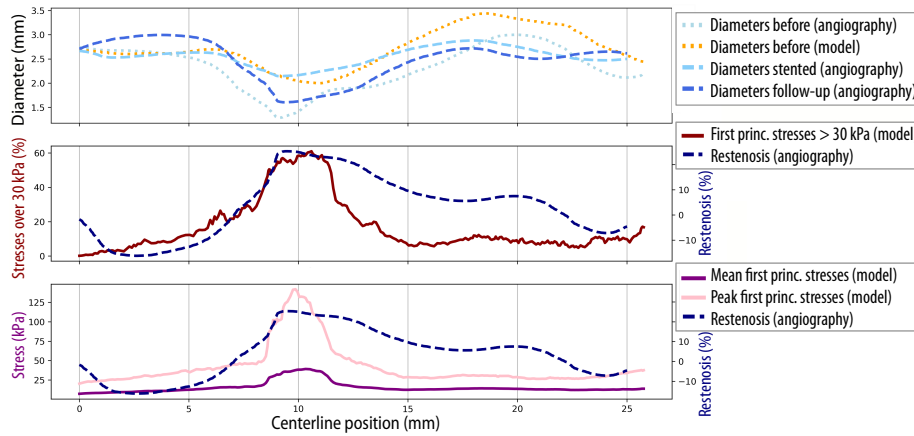


a) Semi-automatic segmentation of the angiography data at end-diastole before stenting, after stenting, and at the follow-up angiography (segmented using AngioPy [69])



b) Computational model of the stented section before and after stenting

c) Computational model after stenting; the first principal stresses are averaged over the orthogonal slices



d) Top: Lumen diameter over the centerline from the angiography data (blue) and the CCTA-based segmentation (orange). The pre-intervention configurations (dotted) are used to scale and match the data. Middle: Comparison of the level of restenosis at follow-up (as seen in the angiography images) and the percentage of first principal stresses over 30 kPa over the cross-section. Bottom: Comparison of restenosis level with mean and peak stresses.

Figure 7: Regional analysis of vessel diameters and stresses after stenting for Patient 2

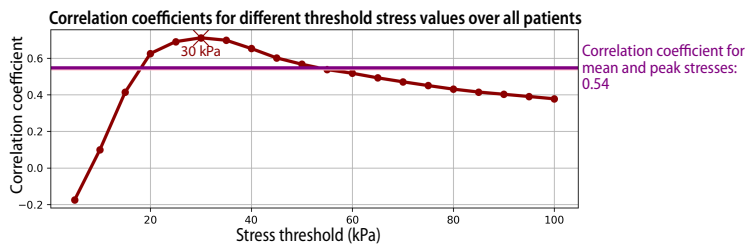


Figure 8: Correlation coefficients for different stress thresholds and for the mean and peak stresses (purple line) over all patients.

For the simulated model, we integrate the first principal stresses of each plane perpendicular to the centerline and divide them by the surface area to obtain the mean stress as a scalar value for each centerline point. We use PyVista for this analysis [70]. Exemplary slices are shown in Fig. 7c). The mean local mechanical stresses in the stented region show a positive linear correlation with the amount of ISR in these regions. We calculate a Pearson correlation coefficient of 0.54 for the data of the three example patients combined. The peak stresses of each plane perpendicular to the centerline (shown in Fig. 7d), bottom) also shows a positive correlation with the amount of ISR, with a correlation coefficient of 0.54. The 95th percentile of the tensional stresses was used instead of the absolute maximum to reduce the impact of local singularities and numerical outliers.

Furthermore, we analyze the correlation between the tissue area experiencing tensional stresses above a certain stress threshold and the amount of restenosis. For each slice along the centerline, we compute the ratio of tissue with stresses above a certain stress threshold to the total slice area. The resulting ratios correlate with the restenosis amount in each centerline position using a Pearson correlation coefficient. We perform this analysis with different stress thresholds between 5 and 100 kPa using the data of the three example patients combined. Figure 8 shows the correlation coefficient for different stress threshold values. The correlation of stresses above a certain threshold with the restenosis amount is highest for 30 kPa with a correlation coefficient of 0.71, i.e., indicating a strong correlation. This value is higher than the correlation coefficient for the mean stress values or peak stresses, indicating a stronger correlation of restenosis with stress values above a certain threshold than with the mean or peak stresses.

3.4. Calcification patterns and stress distributions

We investigate calcification patterns in the cross-sectional view and their influence on the stress distribution post-PCI. In Appendix E, the tensional stress distributions are presented at several cross-sectional views during and after the PCI simulation for all four example lesions. In this section, we highlight two calcification patterns in the example lesions and assess their influence on the specific stress distribution in the cross-section.

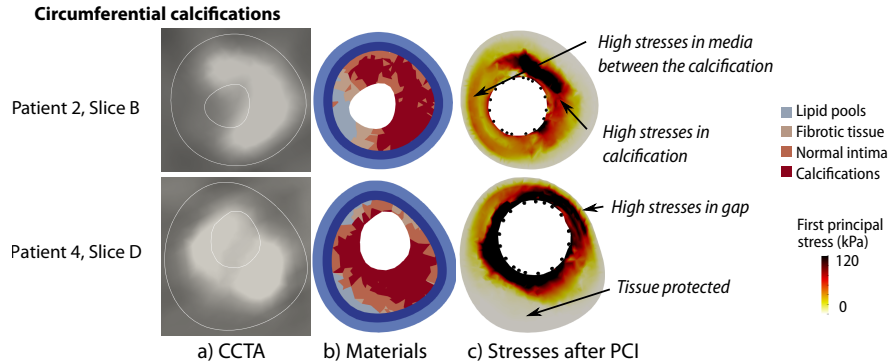


Figure 9: Circumferential calcification pattern a) as seen in the coronary CT angiography image, b) the material distribution in our model and c) the resulting first principal stress distributions after PCI

We define a circumferential calcification pattern as a calcification of more than 180° in the cross-sectional view. In the example lesions, circumferential calcification patterns occur in Patients 2 and 4. Figure 9 shows two extracted cross-sections from Patients 2 and 4 showing the circumferential calcification pattern. We observe peak values of over 120 kPa (black areas) near the circumferential calcifications. The locations of the cross-sections in the respective lesions are given in Appendix E. In the neighboring non-calcified tissue, which is in the two presented cross-sections composed of lipid-rich tissue or fibrotic tissue, the stresses in the intima and media are significantly elevated. The stresses in the calcified parts are also high. However, calcifications possess high mechanical strength and are not susceptible to ISR, as they lack proliferative cells. The media and adventitia outside calcifications are protected against high stresses and strains.

The second specific calcification pattern is the asymmetric block calcification. This pattern in the cross-section can also stem from a longer calcification band along the length of the artery. This pattern occurs in the example patients 1, 2, and 4. Appendix E shows the location of the specific cross-sections and the respective 3D model view. Similarly to the circumferential pattern, Fig. 10 shows the cross-sections of the respective model and the stress distributions after the PCI simulation. Near asymmetric block calcifications, we observe peak values of approximately 60 kPa. Our results suggest higher stresses near and opposing the block calcification. Especially in thin-walled sections on the opposite side, the intima and media experience higher stresses. The tissue behind the calcification seems protected from higher stresses by the calcification.

4. Discussion

This study investigated the influence of specific plaque morphological features on the local mechanical states during and after PCI with stent implantation and the associated occurrence of ISR. Using computational modeling and

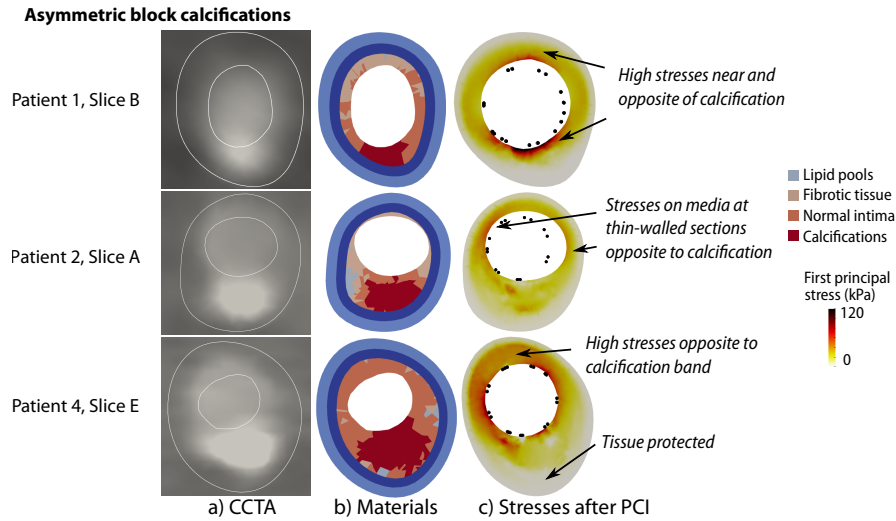


Figure 10: Asymmetric block calcifications a) as seen in the coronary CT angiography image, b) the material distribution in our model and c) the resulting first principal stress distributions after PCI

simulation on four relevant example lesions, a correlation between high-stress areas and the areas where ISR was observed at the follow-up angiography was shown. Furthermore, we have investigated how different plaque morphological features, such as circumferential or asymmetric block calcifications, influence the stress distribution after the stent implantation. The results of this study suggest that the mechanical state during and after PCI, such as stresses on the vessel wall, links specific plaque morphological features with different clinical outcomes. The present study lays the groundwork for consecutive studies with larger patient cohorts and statistical significance to better understand and predict ISR.

4.1. Stress values relevant for ISR

The regional analysis in Section 3.3 showed that average values of 30-40 kPa were reached in the areas with a 20% or more restenosis rate as determined from the angiography images. The computed correlation between the mean tensional stress and the corresponding diameter reduction after PCI was 0.54 for all three patients combined. The same correlation coefficient, 0.54, was computed for the peak tensional stresses with the diameter reduction after PCI.

A qualitative analysis was performed for the 3D stress state in Section 3.2. The results suggest that ISR had appeared in areas with tensional stress values of approximately 40-60 kPa. This higher threshold shows that the mean or peak stress values over cross-sectional slices are insufficient to determine the regions at risk for ISR, but the local values are important. Therefore, we assessed the influence of regions with stresses above a certain threshold on the initiation

of ISR in a further analysis in Section 3.3. We systematically reviewed the correlation of areas with stresses above different thresholds with the ISR rate, assuming that excessive stresses outside of the normal physiological range trigger growth and remodeling processes that can lead to ISR. The analysis led to a correlation of 0.71, i.e., a strong correlation for areas with stresses above 20-40 kPa. The significantly higher correlation coefficient than for the mean or peak stress values supports the hypothesis that there exists a stress threshold critical for ISR rather than a direct correlation with the stress values. Hence, the knowledge of locations at risk for stress peaks is important for ISR prediction.

This study did not aim to conclude a universal critical stress threshold above which ISR is initiated. This threshold is likely individual for different patients and lesions, as multiple factors are involved. In the literature, stress thresholds have been proposed for the plaque rupture. For instance, [71, 72] suggested values of 300-500 kPa, aortic aneurysms rupture at around 450-1000 kPa [73]. However, rupture is a purely mechanical outcome governed by the mechanical state alone, i.e., when stress exceeds strength [16]. In contrast, ISR involves mechanobiological processes, which are determined by the perceived state of cells and set homeostatic targets [16]. Hence, the initiation of ISR is likely governed by a broader range of factors, making it more difficult to pinpoint clear trigger thresholds.

4.2. Influence of plaque morphology on ISR

The stress distributions in the cross-sectional slices highlight the impact of plaque morphology on local stress levels, as shown in Section 3.4. The stresses in the healthy, surrounding tissue of the cross-sections showing specific plaque characteristics, such as circumferential or asymmetric calcifications, were significantly elevated. Peak values of over 120 kPa near the circumferential calcification patterns and approximately 60 kPa near asymmetric block calcifications are reached. These patterns have already been observed to be critical for ISR. Other areas, such as the media and adventitia outside of a block calcification, show significantly lower stresses. The location of the peak stresses after PCI correlated well with the angiography data at follow-up, as shown in Section 3.2, and the documented type of ISR, i.e., focal margin ISR for Patients 1 and 4, diffuse intrastent for Patient 2, and no ISR for Patient 3. The threshold values are chosen based on the top 5 or 20% of the overall stress distribution of each numerical example, respectively. For Patient 3 (no ISR), these values were lower than the other three examples, which showed signs of ISR in the follow-up angiography. We conclude that plaque morphological patterns are relevant to determining the ISR risk. Based on these findings, more extensive studies can be conducted to identify more plaque characteristics at risk for ISR.

4.3. Strengths and limitations

This work assessed the mechanical state of the artery during and after coronary stent implantation, as it is an important factor of ISR that is so far mostly neglected in the literature. Other factors are involved in the development of

ISR, such as denudation at the stent struts, hemodynamic alterations influencing the local intimal wall shear stresses, the type of antiproliferative drugs, and the progression and diffusion of inflammatory and growth factors through the artery wall. These factors have not been studied in this work, but they must be considered to predict ISR.

This study showed the correlation between plaque morphological features and ISR by assessing the mechanical state of four representative lesions. While the small sample size does not allow for statistical generalization, the findings provide valuable mechanistic insights.

We chose the material parameters from experimental data reported in the literature. However, this study did not include an uncertainty quantification of these parameters, which would be an important step toward improving the accuracy of the stress estimates. Furthermore, we applied a GMM-based clustering of the HU values to distinguish between plaque components. This approach is a simplification, as it reduces the complex and continuous microstructural transitions to discrete categories. Therefore, a soft clustering of the plaque materials could be more realistic.

4.4. Clinical relevance and future research

This work found that local mechanical stresses are critical for assessing the individual ISR risk. To assess this correlation, we performed numerical simulations of the stenting procedure and utilized comprehensive clinical data, i.e., CCTA, coronary angiography, and interventional data before, during, and after PCI. These results can be used in future computational studies on stenting and ISR, especially when less clinical data is available.

Insights into plaque morphology patterns at risk for ISR can help the non-invasive assessment of lesions, for instance, using CCTA imaging, in addition to existing risk factors for ISR.

The morphological plaque features could be resolved in more detail using a soft clustering approach. Using GMM clustering, the probability of a distinct HU value belonging to a different material could be used as the basis of a constrained mixture of materials of the respective components, see e.g. [74, 75]. An inverse analysis with corresponding experimental data and microstructural insights on how the materials transform into each other would be beneficial to fine-tune this mapping.

The approach introduced in [20] is applicable for any coronary artery section, independently of its degree of stenosis, plaque composition, and morphology. To further quantify the critical stress thresholds for ISR, we suggest a study with a larger number of lesions. Additionally, a larger patient study should be used to derive statistically relevant correlations between the plaque morphology and tensional stress distribution and eventually predict ISR.

Appendix A. Model generation from imaging data

We create the patient-specific stenotic artery models, as detailed in [20]. The segmentation from CCTA imaging data is done using [76], and we use the coronary angiography imaging data to refine the lumen geometry qualitatively.

We assume that the pathological thickening of the wall affects only the intima. Hence, the media and adventitia are modeled with fixed thicknesses. The remaining intimal tissue is further classified into specific plaque components, as described in Section 2.1. The artery material is modeled as (almost) incompressible, anisotropic, viscoelastic, with a non-linear stress-strain curve. We use a Neo-Hookean base material with exponential fiber contributions to describe the constitutive behavior [77, 78]. The material models and parameters are specified in A.1.

	Base material		Fibers		
	E (MPa)	ν (-)	k_1 (kPa)	k_2 (-)	ϕ ($^\circ$)
Adventitia	0.016	0.45	5.1	15.4	56.3
Media	0.16	0.45	0.64	3.54	5.76
Normal intima	0.16	0.45			
Lipid-rich plaque	0.08	0.45			
Fibrotic plaque	0.16	0.45			
Calcification	1.6	0.45			

Table A.1: Material parameters of the artery model

Appendix B. Gaussian Mixture Model mapping

For the GMM-based mapping of the plaque composition described in Section 2.1, the following tools and specifications are employed. We use the Scikit Learn library [79] to learn the GMM from the HU data of the intima domain and cluster the data accordingly. Each data point, i.e., discrete HU value, is assigned to the Gaussian it most likely belongs to [59]. We use the ‘k-means’ method with pre-defined mean values to initialize the GMM. The means are chosen based on the typical HU ranges for the different plaque components, see e.g. [58] and the number of plaque components is specified to four. Additionally, we use SimpleITK [80] as an interface from the medical imaging data to the mapping.

Appendix C. Patient characteristics

The patient and interventional data for the examples in Section 3 are summarized in Table C.2.

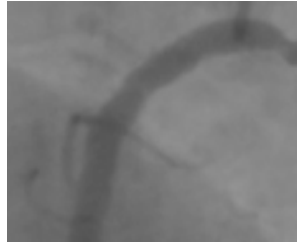
Patient 1	Female, 58y.
<i>Diagnosis</i>	Proximal RCA severely stenosed, stable angina pect
<i>CV risk factors</i>	Smoker, arterial hypertension, hypercholesterolemia
<i>Treatment</i>	(Successful) stenting of the RCA
<i>Follow-up</i>	Restenosis (focal margin)
Patient 2	Male, 71y.
<i>Diagnosis</i>	Medial RCA severely stenosed, exertional dyspnea
<i>CV risk factors</i>	Adiposity, arterial hypertension, hypercholesterolemia
<i>Treatment</i>	Stenting of RCA, post-dilatation was necessary in proximal section
<i>Follow-up</i>	Restenosis (diffuse intrastent)
Patient 3	Female, 68y.
<i>Diagnosis</i>	Triple-vessel coronary artery disease, reduced LV function
<i>CV risk factors</i>	Prior interventions, hypertension, adiposity, hypercholesterolemia
<i>Treatment</i>	Four stents in RCA, post-dilatation in some areas
<i>Follow-up</i>	Good result in stent area, no recurrent treatment necessary
Patient 4	Male, 61y.
<i>Diagnosis</i>	Severe stenosis of proximal, medial and distal RCA
<i>CV risk factors</i>	Family history of CVD, hypercholesterolemia
<i>Treatment</i>	Three stents in RCA, pre- and post-dilatation
<i>Follow-up</i>	ISR in RCA (focal margin)

Table C.2: Patient and interventional data. CV: cardiovascular, RCA: right coronary artery, LV: left ventricular, CVD: cardiovascular disease, ISR: in-stent restenosis

Appendix D. Stent placement and correspondence to angiography data

In the following, we compare the simulation results to the angiography imaging data. We select single frames during the diastole from the respective angiography data. For each patient, Subfigures a) and d) show the configuration before the intervention. Subfigures b) and e) show the angiography image after the intervention and the simulated stented artery. Subfigures c) and f) compare the follow-up angiography with the maximum stresses after the intervention.

Patient 1



a) Before intervention



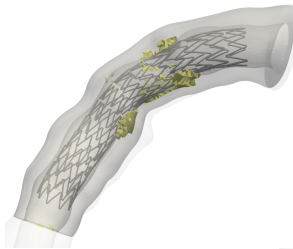
b) After intervention

No image data available

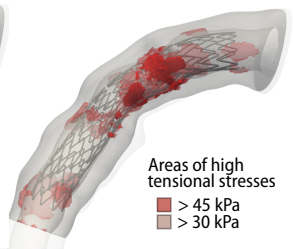
c) ISR (focal margin) at follow-up



d) Stent placement

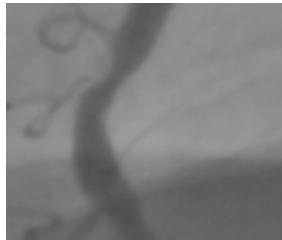


e) Stented artery

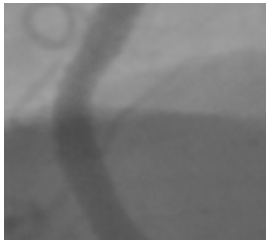


f) Principal stresses after PCI

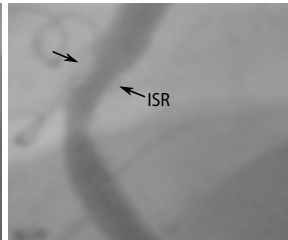
Patient 2



a) Before intervention



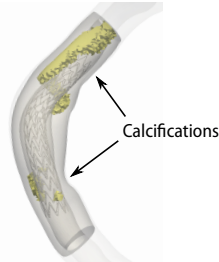
b) After intervention



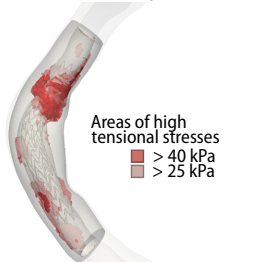
c) ISR at follow-up



d) Stent placement

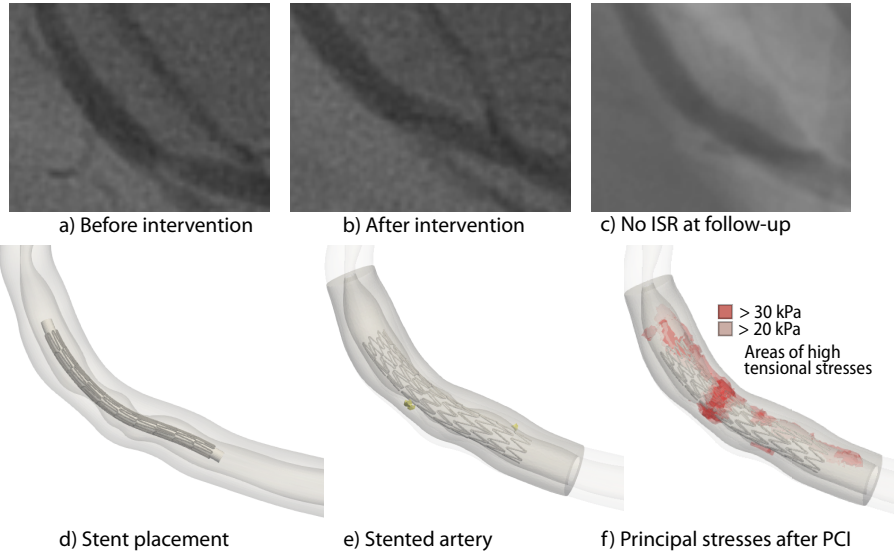


e) Stented artery

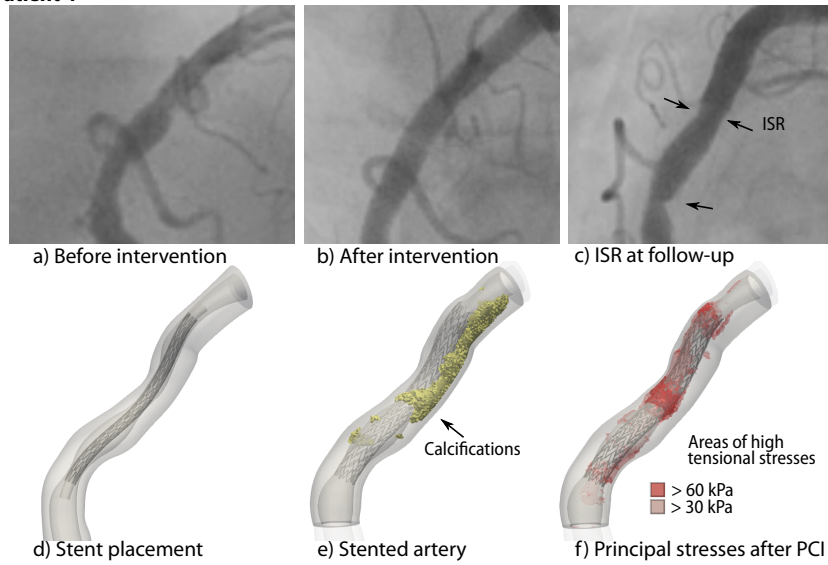


f) Principal stresses after PCI

Patient 3



Patient 4



Appendix E. Patient-specific stress results during and after PCI

Appendix E.1. Stress distribution in cross-sections

In the following, we present the complete results for the stress distributions in cross-sectional slices of the four numerical examples.

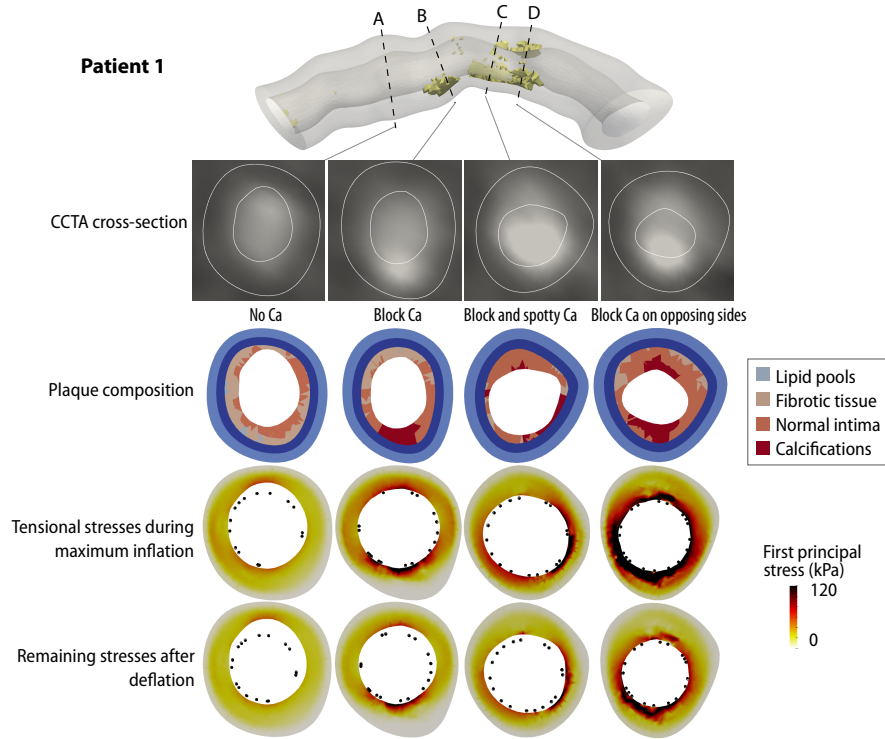


Figure E.11: First principal stress values in selected cross-sections during and after PCI; Patient 1. The plaque morphology is shown in the coronary computed tomography angiography cross-sections and in the model. The stent cross-section is shown as black dots. Ca: Calcification.

Patient 1 shows the following plaque characteristics in the cross-sections: one-sided block calcification (Slice B), small block calcification with scattered calcified particles (Slice C), opposing calcifications (Slice D), see Fig. E.11. During maximum balloon inflation (Fig. E.11, third row), stress peaks can mainly be observed near the calcifications. High stresses occur in the media and adventitia, especially in the thin-walled area next to the larger calcifications in Slice D. After PCI, the stress values are reduced; however, the spatial distribution is similar to the maximum pressure state.

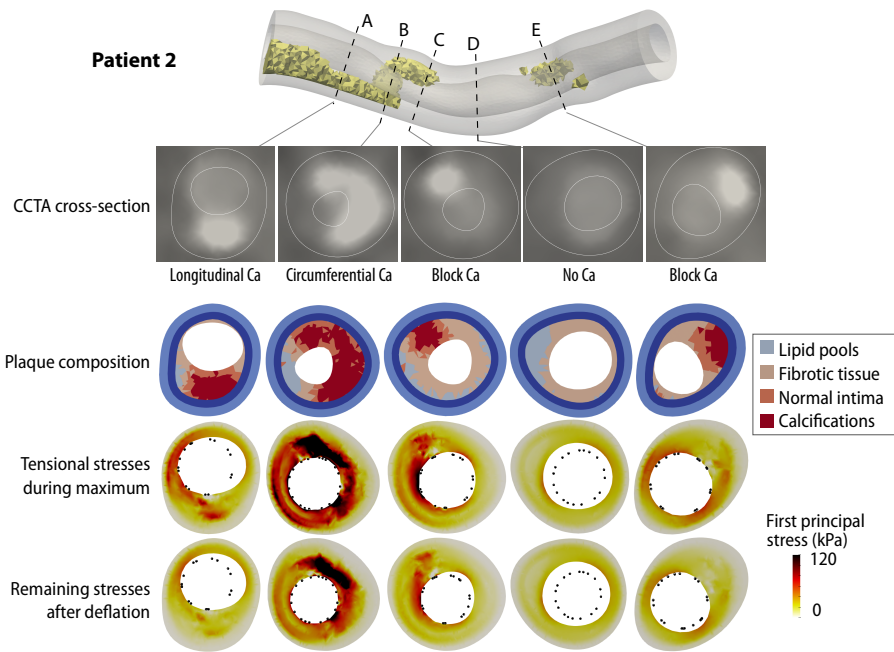


Figure E.12: First principal stress values in selected cross-sections during and after PCI; Patient 2. The plaque morphology is shown in the coronary computed tomography angiography cross-sections and in the model. The stent cross-section is shown as black dots. Ca: Calcification.

Patient 2 shows the following plaque characteristics in the cross-sections: Longitudinal or one-sided block calcifications (Slice A, C, E) and circumferential calcification (Slice B). Slice D shows no calcifications. The highest tensional stresses during and after PCI occur in Slice B, where the calcification pattern switches from a longitudinal band to circumferential. High stresses in the healthy tissue near the circumferential calcification also affect the media and adventitia. In the areas with asymmetric block calcifications, higher stress values occur in the thin-walled areas next to or opposite the calcification.

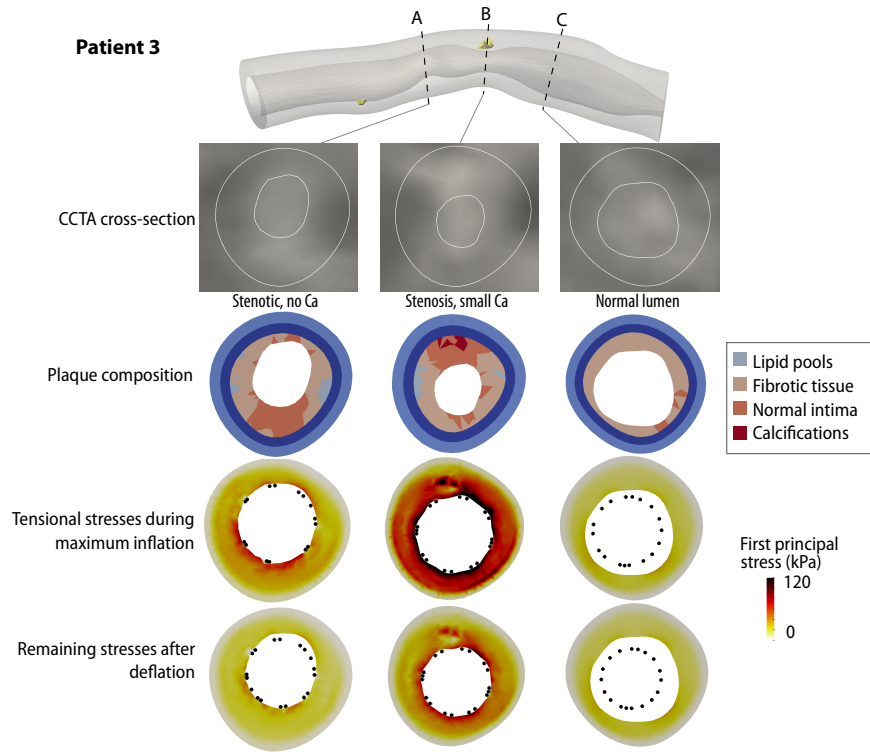


Figure E.13: First principal stress values in selected cross-sections during and after PCI; Patient 3. The plaque morphology is shown in the coronary computed tomography angiography cross-sections and in the model. The stent cross-section is shown as black dots. Ca: Calcification.

Patient 3 shows no significant calcifications; the lesion mainly comprises fibrous tissue. We observe the highest stresses during the maximum balloon inflation in the location of the most severe stenosis. However, the remaining stresses after the balloon withdrawal are reduced drastically and more evenly distributed in the tissue than in the lesions with calcifications.

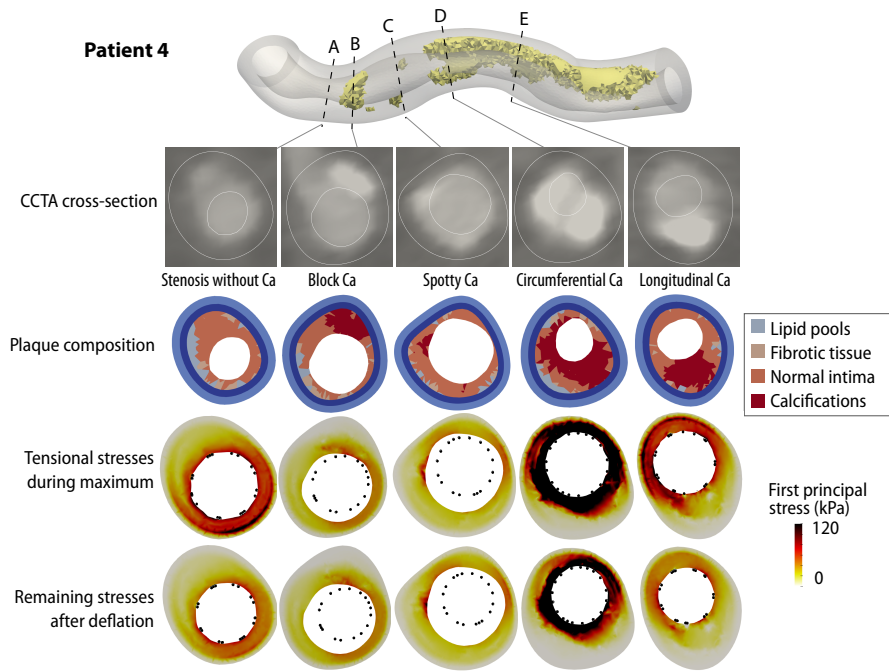


Figure E.14: First principal stress values in selected cross-sections during and after PCI; Patient 4. The plaque morphology is shown in the coronary computed tomography angiography cross-sections and in the model. The stent cross-section is shown as black dots. Ca: Calcification.

The lesion in Patient 4 contains a large calcification, that is, similar to the pattern of Patient 2, arranged longitudinally with a switch to a circumferential pattern. Additionally, in the proximal section, there are smaller calcification blocks. In the proximal part, we observe high stresses opposite of asymmetric calcifications, especially in the thin-walled sections. The highest stress values occur in the section of the circumferential calcification. The media and adventitia experience lower stresses in calcified areas.

References

- [1] R. A. Byrne, M. Joner, A. Kastrati, Stent thrombosis and restenosis: What have we learned and where are we going? The Andreas Grüntzig Lecture ESC 2014, *European Heart Journal* 36 (47) (2015) 3320–3331. doi:10.1093/eurheartj/ehv511.
- [2] S. Cassese, R. A. Byrne, T. Tada, S. Pinieck, M. Joner, T. Ibrahim, L. A. King, M. Fusaro, K.-L. Laugwitz, A. Kastrati, Incidence and predictors of restenosis after coronary stenting in 10 004 patients with surveillance angiography, *Heart* 100 (2) (2014) 153–159. doi:10.1136/heartjnl-2013-304933.
- [3] N. Shafiabadi Hassani, L. C. Ogliari, P. R. Vieira de Oliveira Salerno, G. T. R. Pereira, M. H. Ribeiro, L. A. Palma Dallan, In-Stent Restenosis Overview: From Intravascular Imaging to Optimal Percutaneous Coronary Intervention Management, *Medicina* 60 (4) (2024) 549. doi:10.3390/medicina60040549.
- [4] R. Adolf, I. Krinke, J. Datz, S. Cassese, A. Kastrati, M. Joner, H. Schunkert, W. Wall, M. Hadamitzky, L.-C. Engel, Specific calcium deposition on pre-procedural CCTA at the time of percutaneous coronary intervention predicts in-stent restenosis in symptomatic patients, *Journal of Cardiovascular Computed Tomography* (Oct. 2024). doi:10.1016/j.jcct.2024.09.010.
- [5] Y. Suzuki, M. Uehara, H. Ando, A. Suzuki, A. Murata, H. Matsuda, T. Tokuda, T. Amano, Clinical outcomes of percutaneous coronary intervention for severely calcified lesions: Comparison between the morphologies of severely calcified coronary lesions, *Heart and Vessels* (Sep. 2024). doi:10.1007/s00380-024-02466-7.
- [6] L. P. Dawson, J. Layland, High-Risk Coronary Plaque Features: A Narrative Review, *Cardiology and Therapy* 11 (3) (2022) 319–335. doi:10.1007/s40119-022-00271-9.
- [7] N. Iraqi, B. L. Nørgaard, D. Dey, J. Abdulla, Influence of plaque characteristics by coronary computed tomography angiography on lesion-specific ischemia: A systematic review and meta-analysis, *European Radiology* (Mar. 2025). doi:10.1007/s00330-025-11516-1.
- [8] A. Tajima, F. Bouisset, H. Ohashi, K. Sakai, T. Mizukami, M. L. Rizzini, D. Gallo, C. Chiastra, U. Morbiducci, Z. A. Ali, J. C. Spratt, H. Ando, T. Amano, P. Kitslaar, A. Wilgenhof, J. Sonck, B. De Bruyne, C. Collet, Advanced CT Imaging for the Assessment of Calcific Coronary Artery Disease and PCI Planning, *Journal of the Society for Cardiovascular Angiography & Interventions* 3 (3, Part B) (2024) 101299. doi:10.1016/j.jscai.2024.101299.
- [9] U. Guldener, T. Kessler, M. von Scheidt, J. S. Hawe, B. Gerhard, D. Maier, M. Lachmann, K.-L. Laugwitz, S. Cassese, A. W. Schömig, A. Kastrati,

- H. Schunkert, Machine Learning Identifies New Predictors on Restenosis Risk after Coronary Artery Stenting in 10,004 Patients with Surveillance Angiography, *Journal of Clinical Medicine* 12 (8) (2023) 2941. doi:10.3390/jcm12082941.
- [10] C. Lally, P. J. Prendergast, Simulation of In-stent Restenosis for the Design of Cardiovascular Stents, in: G. A. Holzapfel, R. W. Ogden (Eds.), *Mechanics of Biological Tissue*, Springer-Verlag, Berlin/Heidelberg, 2006, pp. 255–267. doi:10.1007/3-540-31184-X_18.
- [11] G. A. Rodriguez-Granillo, P. W. Serruys, H. M. Garcia-Garcia, J. Aoki, M. Valgimigli, C. A. G. van Mieghem, E. McFadden, P. P. T. de Jaegere, P. de Feyter, Coronary artery remodelling is related to plaque composition, *Heart* 92 (3) (2006) 388–391. doi:10.1136/hrt.2004.057810.
- [12] D. Liu, Z. Xue, J. Qi, L. Yin, B. Duan, L. Wu, K. Yang, B. Gao, Q. Cao, J. Mi, Risk factors for in-stent restenosis of sirolimus-coated stents in coronary intervention for patients with unstable angina, *Scientific Reports* 14 (1) (2024) 2537. doi:10.1038/s41598-024-52567-6.
- [13] L. Irons, A. C. Estrada, J. D. Humphrey, Intracellular signaling control of mechanical homeostasis in the aorta, *Biomechanics and Modeling in Mechanobiology* (Jul. 2022). doi:10.1007/s10237-022-01593-2.
- [14] J. F. Eichinger, L. J. Haeusel, D. Paukner, R. C. Aydin, J. D. Humphrey, C. J. Cyron, Mechanical homeostasis in tissue equivalents: A review, *Biomechanics and Modeling in Mechanobiology* (Mar. 2021). doi:10.1007/s10237-021-01433-9.
- [15] J. F. Eichinger, D. Paukner, R. C. Aydin, W. A. Wall, J. D. Humphrey, C. J. Cyron, What do cells regulate in soft tissues on short time scales?, *Acta Biomaterialia* 134 (2021) 348–356. doi:10.1016/j.actbio.2021.07.054.
- [16] J. D. Humphrey, M. A. Schwartz, Vascular Mechanobiology: Homeostasis, Adaptation, and Disease, *Annual Review of Biomedical Engineering* 23 (1) (2021) 1–27. doi:10.1146/annurev-bioeng-092419-060810.
- [17] A. Farb, D. K. Weber, F. D. Kolodgie, A. P. Burke, R. Virmani, Morphological Predictors of Restenosis After Coronary Stenting in Humans, *Circulation* 105 (25) (2002) 2974–2980. doi:10.1161/01.CIR.0000019071.72887.BD.
- [18] A. J. Brown, Z. Teng, P. C. Evans, J. H. Gillard, H. Samady, M. R. Bennett, Role of biomechanical forces in the natural history of coronary atherosclerosis, *Nature Reviews Cardiology* 13 (4) (2016) 210–220. doi:10.1038/nrcardio.2015.203.
- [19] P. Mortier, J. J. Wentzel, G. De Santis, C. Chiastra, F. Migliavacca, M. De Beule, Y. Louvard, G. Dubini, Patient-specific computer modelling of coronary bifurcation stenting: The John Doe programme, *EuroIntervention* 11 (V) (2015) V35–V39. doi:10.4244/EIJV11SVA8.

- [20] J. C. Datz, I. Steinbrecher, C. Meier, N. Hagemeyer, L.-C. Engel, A. Popp, M. R. Pfaller, H. Schunkert, W. A. Wall, Patient-specific coronary angioplasty simulations — A mixed-dimensional finite element modeling approach, *Computers in Biology and Medicine* 189 (2025) 109914. doi:10.1016/j.compbiomed.2025.109914.
- [21] S. Morlacchi, S. G. Colleoni, R. Cárdenes, C. Chiastra, J. L. Diez, I. Larrabide, F. Migliavacca, Patient-specific simulations of stenting procedures in coronary bifurcations: Two clinical cases, *Medical Engineering & Physics* 35 (9) (2013) 1272–1281. doi:10.1016/j.medengphy.2013.01.007.
- [22] F. Auricchio, M. Conti, A. Ferrara, S. Morganti, A. Reali, Patient-specific finite element analysis of carotid artery stenting: A focus on vessel modeling, *International Journal for Numerical Methods in Biomedical Engineering* 29 (6) (2013) 645–664. doi:10.1002/cnm.2511.
- [23] G. E. Ragkousis, N. Curzen, N. W. Bressloff, Computational Modelling of Multi-folded Balloon Delivery Systems for Coronary Artery Stenting: Insights into Patient-Specific Stent Malapposition, *Annals of Biomedical Engineering* 43 (8) (2015) 1786–1802. doi:10.1007/s10439-014-1237-8.
- [24] G. E. Ragkousis, N. Curzen, N. W. Bressloff, Simulation of longitudinal stent deformation in a patient-specific coronary artery, *Medical Engineering & Physics Volume 36 (Issue 4)* (2014) 467–476. doi:10.1016/j.medengphy.2014.02.004.
- [25] P. Mortier, G. A. Holzapfel, M. De Beule, D. Van Loo, Y. Taeymans, P. Segers, P. Verdonck, B. Verhegghé, A Novel Simulation Strategy for Stent Insertion and Deployment in Curved Coronary Bifurcations: Comparison of Three Drug-Eluting Stents, *Annals of Biomedical Engineering* 38 (1) (2010) 88–99. doi:10.1007/s10439-009-9836-5.
- [26] H. Zahedmanesh, D. John Kelly, C. Lally, Simulation of a balloon expandable stent in a realistic coronary artery—Determination of the optimum modelling strategy, *Journal of Biomechanics* 43 (11) (2010) 2126–2132. doi:10.1016/j.jbiomech.2010.03.050.
- [27] F. J. Gijssen, F. Migliavacca, S. Schievano, L. Soggi, L. Petrini, A. Thury, J. J. Wentzel, A. F. van der Steen, P. W. Serruys, G. Dubini, Simulation of stent deployment in a realistic human coronary artery, *BioMedical Engineering OnLine* 7 (1) (2008) 23. doi:10.1186/1475-925X-7-23.
- [28] C. Conway, J. P. McGarry, E. R. Edelman, P. E. McHugh, Numerical Simulation of Stent Angioplasty with Predilatation: An Investigation into Lesion Constitutive Representation and Calcification Influence, *Annals of Biomedical Engineering* 45 (9) (2017) 2244–2252. doi:10.1007/s10439-017-1851-3.

- [29] A. Karimi, M. Navidbakhsh, H. Yamada, R. Razaghi, A nonlinear finite element simulation of balloon expandable stent for assessment of plaque vulnerability inside a stenotic artery, *Medical & Biological Engineering & Computing* 52 (7) (2014) 589–599. doi:10.1007/s11517-014-1163-9.
- [30] I. Pericevic, C. Lally, D. Toner, D. J. Kelly, The influence of plaque composition on underlying arterial wall stress during stent expansion: The case for lesion-specific stents, *Medical Engineering & Physics* 31 (4) (2009) 428–433. doi:10.1016/j.medengphy.2008.11.005.
- [31] C. Conway, J. P. McGarry, P. E. McHugh, Modelling of Atherosclerotic Plaque for Use in a Computational Test-Bed for Stent Angioplasty, *Annals of Biomedical Engineering* 42 (12) (2014) 2425–2439. doi:10.1007/s10439-014-1107-4.
- [32] B. Helou, A. Bel-Brunon, C. Dupont, W. Ye, C. Silvestro, M. Rochette, A. Lucas, A. Kaladji, P. Haigron, Influence of balloon design, plaque material composition, and balloon sizing on acute post angioplasty outcomes: An implicit finite element analysis, *International Journal for Numerical Methods in Biomedical Engineering* 37 (8) (2021) e3499. doi:10.1002/cnm.3499.
- [33] R. R. Deokar, B. E. Klamecki, Computational Modeling and Comparative Tissue Damage Analysis of Angioplasty and Orbital Atherectomy Interventional Procedures, *Journal of Medical Devices* 11 (021006) (May 2017). doi:10.1115/1.4036299.
- [34] L. Wei, Q. Chen, Z. Li, Influences of plaque eccentricity and composition on the stent–plaque–artery interaction during stent implantation, *Biomechanics and Modeling in Mechanobiology* 18 (1) (2019) 45–56. doi:10.1007/s10237-018-1066-z.
- [35] S. Morlacchi, G. Pennati, L. Petrini, G. Dubini, F. Migliavacca, Influence of plaque calcifications on coronary stent fracture: A numerical fatigue life analysis including cardiac wall movement, *Journal of Biomechanics* 47 (4) (2014) 899–907. doi:10.1016/j.jbiomech.2014.01.007.
- [36] F. Iannaccone, N. Debusschere, S. De Bock, M. De Beule, D. Van Loo, F. Vermassen, P. Segers, B. Verhegghe, The influence of vascular anatomy on carotid artery stenting: A parametric study for damage assessment, *Journal of Biomechanics* 47 (4) (2014) 890–898. doi:10.1016/j.jbiomech.2014.01.008.
- [37] T. R. Welch, R. C. Eberhart, S. Banerjee, C.-J. Chuong, Mechanical Interaction of an Expanding Coiled Stent with a Plaque-Containing Arterial Wall: A Finite Element Analysis, *Cardiovascular Engineering and Technology* 7 (1) (2016) 58–68. doi:10.1007/s13239-015-0249-3.

- [38] D. E. Kiousis, T. C. Gasser, G. A. Holzapfel, A Numerical Model to Study the Interaction of Vascular Stents with Human Atherosclerotic Lesions, *Annals of Biomedical Engineering* 35 (11) (2007) 1857–1869. doi:10.1007/s10439-007-9357-z.
- [39] A. Corti, L. Dal Ferro, A. C. Akyildiz, F. Migliavacca, S. McGinty, C. Chiastra, Plaque heterogeneity influences in-stent restenosis following drug-eluting stent implantation: Insights from patient-specific multiscale modelling, *Journal of Biomechanics* 179 (2025) 112485. doi:10.1016/j.jbiomech.2024.112485.
- [40] S. Samant, W. Wu, S. Zhao, B. Khan, M. Sharzehee, A. Panagopoulos, J. Makadia, T. Mickley, A. Bicek, D. Boismier, Y. Murasato, Y. S. Chatzizisis, Computational and experimental mechanical performance of a new everolimus-eluting stent purpose-built for left main interventions, *Scientific Reports* 11 (1) (2021) 8728. doi:10.1038/s41598-021-87908-2.
- [41] C. Chiastra, W. Wu, B. Dickerhoff, A. Aleiou, G. Dubini, H. Otake, F. Migliavacca, J. F. LaDisa, Computational replication of the patient-specific stenting procedure for coronary artery bifurcations: From OCT and CT imaging to structural and hemodynamics analyses, *Journal of Biomechanics* 49 (11) (2016) 2102–2111. doi:10.1016/j.jbiomech.2015.11.024.
- [42] A. Mastrofini, M. Marino, E. Karlöf, U. Hedin, T. C. Gasser, On the Impact of Residual Strains in the Stress Analysis of Patient-Specific Atherosclerotic Carotid Vessels: Predictions Based on the Homogenous Stress Hypothesis, *Annals of Biomedical Engineering* 52 (5) (2024) 1347–1358. doi:10.1007/s10439-024-03458-4.
- [43] N. Curcio, A. Rosato, D. Mazzaccaro, G. Nano, M. Conti, G. Matrone, 3D patient-specific modeling and structural finite element analysis of atherosclerotic carotid artery based on computed tomography angiography, *Scientific Reports* 13 (1) (2023) 19911. doi:10.1038/s41598-023-46949-5.
- [44] J. L. Warren, J. E. Yoo, C. A. Meyer, D. S. Molony, H. Samady, H. N. Hayenga, Automated finite element approach to generate anatomical patient-specific biomechanical models of atherosclerotic arteries from virtual histology-intravascular ultrasound, *Frontiers in Medical Technology* 4 (Nov. 2022). doi:10.3389/fmedt.2022.1008540.
- [45] A. C. Akyildiz, L. Speelman, H. van Brummelen, M. A. Gutiérrez, R. Virmani, A. van der Lugt, A. F. van der Steen, J. J. Wentzel, F. J. Gijsen, Effects of intima stiffness and plaque morphology on peak cap stress, *BioMedical Engineering OnLine* 10 (1) (2011) 25. doi:10.1186/1475-925X-10-25.
- [46] A. Corti, M. Stefanati, M. Leccardi, O. De Filippo, A. Depaoli, P. Cerveri, F. Migliavacca, V. Corino, J. F. Rodriguez Matas, L. Mainardi, G. Dubini, Predicting High-Risk Patients: A Biomechanical-Based Machine Learning

Approach for Coronary Vulnerable Plaques Detection, in: 2024 Computing in Cardiology Conference, 2024. doi:10.22489/CinC.2024.314.

- [47] K. Kadry, M. L. Olender, D. Marlevi, E. R. Edelman, F. R. Nezami, A platform for high-fidelity patient-specific structural modelling of atherosclerotic arteries: From intravascular imaging to three-dimensional stress distributions, *Journal of The Royal Society Interface* 18 (182) (2021) 20210436. doi:10.1098/rsif.2021.0436.
- [48] Y. Gharaibeh, J. Lee, D. Prabhu, P. Dong, V. N. Zimin, L. A. Dallan, H. Bezerra, L. Gu, D. Wilson, Co-registration of pre- and post-stent intravascular OCT images for validation of finite element model simulation of stent expansion, in: *Medical Imaging 2020: Biomedical Applications in Molecular, Structural, and Functional Imaging*, Vol. 11317, SPIE, 2020, pp. 306–316. doi:10.1117/12.2550212.
- [49] S. Zhao, W. Wu, S. Samant, B. Khan, G. S. Kassab, Y. Watanabe, Y. Murasato, M. Sharzehee, J. Makadia, D. Zolty, A. Panagopoulos, F. Burzotta, F. Migliavacca, T. W. Johnson, T. Lefevre, J. F. Lassen, E. S. Brilakis, D. L. Bhatt, G. Dangas, C. Chiastra, G. Stankovic, Y. Louvard, Y. S. Chatzizisis, Patient-specific computational simulation of coronary artery bifurcation stenting, *Scientific Reports* 11 (1) (2021) 16486. doi:10.1038/s41598-021-95026-2.
- [50] G. Poletti, L. Antonini, L. Mandelli, P. Tsompou, G. S. Karanasiou, M. I. Papafaklis, L. K. Michalis, D. I. Fotiadis, L. Petrini, G. Pennati, Towards a Digital Twin of Coronary Stenting: A Suitable and Validated Image-Based Approach for Mimicking Patient-Specific Coronary Arteries, *Electronics* 11 (3) (2022) 502. doi:10.3390/electronics11030502.
- [51] L. Antonini, G. Poletti, G. S. Karanasiou, A. Sakellarios, D. I. Fotiadis, L. Petrini, G. Pennati, F. Berti, A computational workflow for modeling complex patient-specific coronary stenting cases, *Computer Methods and Programs in Biomedicine* (2024) 108527doi:10.1016/j.cmpb.2024.108527.
- [52] P. Dong, H. Mozafari, D. Prabhu, H. G. Bezerra, D. L. Wilson, L. Gu, Optical Coherence Tomography-Based Modeling of Stent Deployment in Heavily Calcified Coronary Lesion, *Journal of Biomechanical Engineering* 142 (051012) (Jan. 2020). doi:10.1115/1.4045285.
- [53] Z.-M. Fan, X. Liu, C.-F. Du, A.-Q. Sun, N. Zhang, Z.-M. Fan, Y.-B. Fan, X.-Y. Deng, Plaque components affect wall stress in stented human carotid artery: A numerical study, *Acta Mechanica Sinica* 32 (6) (2016) 1149–1154. doi:10.1007/s10409-016-0572-4.
- [54] H. A. Nieuwstadt, A. C. Akyildiz, L. Speelman, R. Virmani, A. van der Lugt, A. F. W. van der Steen, J. J. Wentzel, F. J. H. Gijssen, The influence of axial image resolution on atherosclerotic plaque

- stress computations, *Journal of Biomechanics* 46 (4) (2013) 689–695. doi:10.1016/j.jbiomech.2012.11.042.
- [55] G. Holzapfel, M. Stadler, T. Gasser, Changes in the mechanical environment of stenotic arteries during interaction with stents: Computational assessment of parametric stent designs, *Journal of biomechanical engineering* 127 (2005) 166–80.
- [56] D. Andreini, C. Collet, J. Leipsic, K. Nieman, M. Bittencourt, J. De Mey, N. Buls, Y. Onuma, S. Mushtaq, E. Conte, A. L. Bartorelli, G. Stefanini, J. Sonck, P. Knaapen, B. Ghoshhajra, P. Serruys, Pre-procedural planning of coronary revascularization by cardiac computed tomography: An expert consensus document of the Society of Cardiovascular Computed Tomography, *Journal of Cardiovascular Computed Tomography* 16 (6) (2022) 558–572. doi:10.1016/j.jcct.2022.08.003.
- [57] L. J. Shaw, R. Blankstein, J. J. Bax, M. Ferencik, M. S. Bittencourt, J. K. Min, D. S. Berman, J. Leipsic, T. C. Villines, D. Dey, S. Al’Aref, M. C. Williams, F. Lin, L. Baskaran, H. Litt, D. Litmanovich, R. Cury, U. Gianni, I. Van Den Hoogen, A. R. Van Rosendael, M. Budoff, H.-J. Chang, H. E. Hecht, G. Feuchtner, A. Ahmadi, B. B. Ghoshajra, D. Newby, Y. Chandrashekar, J. Narula, Society of Cardiovascular Computed Tomography / North American Society of Cardiovascular Imaging – Expert Consensus Document on Coronary CT Imaging of Atherosclerotic Plaque, *Journal of Cardiovascular Computed Tomography* 15 (2) (2021) 93–109. doi:10.1016/j.jcct.2020.11.002.
- [58] K. Nieman, H. M. García-García, A. Hideo-Kajita, C. Collet, D. Dey, F. Pugliese, G. Weissman, J. G. P. Tijssen, J. Leipsic, M. P. Opol-ski, M. Ferencik, M. T. Lu, M. C. Williams, N. Bruining, P. J. Blanco, P. Maurovich-Horvat, S. Achenbach, Standards for quantitative assessments by coronary computed tomography angiography (CCTA): An expert consensus document of the society of cardiovascular computed tomography (SCCT), *Journal of Cardiovascular Computed Tomography* (Jun. 2024). doi:10.1016/j.jcct.2024.05.232.
- [59] L. Gupta, T. Sortrakul, A gaussian-mixture-based image segmentation algorithm, *Pattern Recognition* 31 (3) (1998) 315–325. doi:10.1016/S0031-3203(97)00045-9.
- [60] L. Athanasiou, G. Rigas, A. I. Sakellarios, T. P. Exarchos, P. K. Siogkas, C. V. Bourantas, H. M. Garcia-Garcia, P. A. Lemos, B. A. Falcao, L. K. Michalis, O. Parodi, F. Vozzi, D. I. Fotiadis, Three-dimensional reconstruction of coronary arteries and plaque morphology using CT angiography – comparison and registration with IVUS, *BMC Medical Imaging* 16 (1) (2016) 9. doi:10.1186/s12880-016-0111-6.
- [61] O. Klass, S. Kleinhans, M. J. Walker, M. Olszewski, S. Feuerlein, M. Juchems, M. H. K. Hoffmann, Coronary plaque imaging with 256-slice

- multidetector computed tomography: Interobserver variability of volumetric lesion parameters with semiautomatic plaque analysis software, *The International Journal of Cardiovascular Imaging* 26 (6) (2010) 711–720. doi:10.1007/s10554-010-9614-3.
- [62] S. Voros, S. Rinehart, Z. Qian, G. Vazquez, H. Anderson, L. Murrieta, C. Wilmer, H. Carlson, K. Taylor, W. Ballard, D. Karpaliotis, A. Kalynych, C. Brown, Prospective Validation of Standardized, 3-Dimensional, Quantitative Coronary Computed Tomographic Plaque Measurements Using Radiofrequency Backscatter Intravascular Ultrasound as Reference Standard in Intermediate Coronary Arterial Lesions, *JACC: Cardiovascular Interventions* 4 (2) (2011) 198–208. doi:10.1016/j.jcin.2010.10.008.
- [63] M. A. de Graaf, A. Broersen, P. H. Kitslaar, C. J. Roos, J. Dijkstra, B. P. F. Lelieveldt, J. W. Jukema, M. J. Schalij, V. Delgado, J. J. Bax, J. H. C. Reiber, A. J. Scholte, Automatic quantification and characterization of coronary atherosclerosis with computed tomography coronary angiography: Cross-correlation with intravascular ultrasound virtual histology, *The International Journal of Cardiovascular Imaging* 29 (5) (2013) 1177–1190. doi:10.1007/s10554-013-0194-x.
- [64] 4C, 4C: A Comprehensive Multi-Physics Simulation Framework (2024). URL <https://www.4c-multiphysics.org>
- [65] Biomatrix Alpha™, Biosensors International, Morges, Switzerland.
- [66] BeamMe Authors, BeamMe - A general purpose 3D beam finite element input generator. URL <https://github.com/beamme-py/beamme>
- [67] I. Steinbrecher, N. Hagemeyer, C. Meier, A. Popp, A consistent mixed-dimensional coupling approach for 1D Cosserat beams and 2D surfaces in 3D space, *Computational Mechanics* (Jun. 2025). doi:10.1007/s00466-025-02647-9.
- [68] J. D. Humphrey, Vascular Adaptation and Mechanical Homeostasis at Tissue, Cellular, and Sub-cellular Levels, *Cell Biochemistry and Biophysics* 50 (2) (2008) 53–78. doi:10.1007/s12013-007-9002-3.
- [69] T. Mahendiran, D. Thanou, O. Senouf, Y. Jamaa, S. Fournier, B. De Bruyne, E. Abbé, O. Muller, E. Andò, *AngioPy* Segmentation: An open-source, user-guided deep learning tool for coronary artery segmentation, *International Journal of Cardiology* 418 (2025) 132598. doi:10.1016/j.ijcard.2024.132598.
- [70] C. B. Sullivan, A. A. Kaszynski, *PyVista*: 3D plotting and mesh analysis through a streamlined interface for the Visualization Toolkit (VTK), *Journal of Open Source Software* 4 (37) (2019) 1450. doi:10.21105/joss.01450.

- [71] G. A. Holzapfel, J. J. Mulvihill, E. M. Cunnane, M. T. Walsh, Computational approaches for analyzing the mechanics of atherosclerotic plaques: A review, *Journal of Biomechanics* 47 (4) (2014) 859–869. doi:10.1016/j.jbiomech.2014.01.011.
- [72] B. R. Kwak, M. Bäck, M.-L. Bochaton-Piallat, G. Caligiuri, M. J. Daemen, P. F. Davies, I. E. Hofer, P. Holvoet, H. Jo, R. Krams, S. Lehoux, C. Monaco, S. Steffens, R. Virmani, C. Weber, J. J. Wentzel, P. C. Evans, Biomechanical factors in atherosclerosis: Mechanisms and clinical implications, *European Heart Journal* 35 (43) (2014) 3013–3020. doi:10.1093/eurheartj/ehu353.
- [73] J. D. Humphrey, G. A. Holzapfel, Mechanics, mechanobiology, and modeling of human abdominal aorta and aneurysms, *Journal of Biomechanics* 45 (5) (2012) 805–814. doi:10.1016/j.jbiomech.2011.11.021.
- [74] J. D. Humphrey, Constrained Mixture Models of Soft Tissue Growth and Remodeling – Twenty Years After, *Journal of Elasticity* 145 (1) (2021) 49–75. doi:10.1007/s10659-020-09809-1.
- [75] C. J. Cyron, R. C. Aydin, J. D. Humphrey, A homogenized constrained mixture (and mechanical analog) model for growth and remodeling of soft tissue, *Biomechanics and Modeling in Mechanobiology* 15 (6) (2016) 1389–1403. doi:10.1007/s10237-016-0770-9.
- [76] A. Updegrove, N. M. Wilson, J. Merkow, H. Lan, A. L. Marsden, S. C. Shadden, SimVascular: An Open Source Pipeline for Cardiovascular Simulation, *Annals of Biomedical Engineering* 45 (3) (2017) 525–541. doi:10.1007/s10439-016-1762-8.
- [77] T. C. Gasser, G. A. Holzapfel, Finite Element Modeling of Balloon Angioplasty by Considering Overstretch of Remnant Non-diseased Tissues in Lesions, *Computational Mechanics* 40 (1) (2007) 47–60. doi:10.1007/s00466-006-0081-6.
- [78] G. A. Holzapfel, G. Sommer, C. T. Gasser, P. Regitnig, Determination of layer-specific mechanical properties of human coronary arteries with nonatherosclerotic intimal thickening and related constitutive modeling, *American Journal of Physiology-Heart and Circulatory Physiology* 289 (5) (2005) H2048–H2058. doi:10.1152/ajpheart.00934.2004.
- [79] F. Pedregosa, G. Varoquaux, A. Gramfort, V. Michel, B. Thirion, O. Grisel, M. Blondel, P. Prettenhofer, R. Weiss, V. Dubourg, J. Vanderplas, A. Passos, D. Cournapeau, Scikit-learn: Machine Learning in Python.
- [80] B. C. Lowekamp, D. T. Chen, L. Ibanez, D. Blezek, The Design of SimpleITK, *Frontiers in Neuroinformatics* 7 (Dec. 2013). doi:10.3389/fninf.2013.00045.